IEEE Access
Multidisciplinary | Rapid Review | Open Access Journal

Received January 12, 2019, accepted February 2, 2019, date of publication March 4, 2019, date of current version April 2, 2019.

Digital Object Identifier 10.1109/ACCESS.2019.2899346

Analyzing Temperature Rise and Fluid Flow of High-Power-Density and High-Voltage Induction Motor in the Starting Process

YUNYAN XIA, YONGSEN HAN, YONGMING XU, AND MENGMENG AI
School of Electrical and Electronic Engineering, Harbin University of Science and Technology, Harbin 150080, China

Corresponding author: Yunyan Xia (yunyan_x@163.com)

This work was supported in part by the National Nature Science Foundation of China under Grant 51807043 and in part by the Heilongjiang Province Youth Innovative Talent Training Program under Grant UNPYSCT-2018215.

ABSTRACT Transient characteristics in the starting process play an important role in the design and operation of high-power-density and high-voltage induction motor. A field–circuit coupling model is proposed to analyze the transient fluid flow and temperature rise of a YJKK 500-4 2500 kW HPDHV induction motor in the starting process. The wind resistance network model is built to investigate the transient fluid flow and is used to obtain the heat dissipation boundary condition of the transient temperature calculation. The transient electric current is the key to the heat source of the temperature distribution and is calculated by the dynamic mathematical model. According to the obtained heat dissipation boundary condition and heat source, the 3-D fluid–solid coupling model is solved to obtain the transient temperature distribution. Moreover, the highest temperature rise in the starting process is greatly affected by the load. The simulation results show that the smaller fluid flow and the starting current make the winding temperature rise rapidly before the rotating speed of the motor reaches the rated value. When the load is much heavier, the starting time becomes longer and the winding temperature in the starting process will rise rapidly. The experimental results indicate that the proposed model is validated.

INDEX TERMS Induction motor, temperature rise, fluid flow, starting characteristic.

I. INTRODUCTION

The high-power-density and high-voltage (HPDHV) induction motor is helpful for the improvement of work efficiency, and power density, compared with the traditional high-voltage induction motor. However, as the increased power density and electromagnetic load, the heating problem may be more serious in the HPDHV induction motor. Usually, the temperature distribution in the steady-state operation is easy to be obtained and is used to monitor the heating state of the induction motor. In addition, the starting process of induction motor may also have a great impact on the heating state. During the starting process, the temperature rise of the stator and rotor windings may reach a higher value, accelerating the thermal aging of the motor insulation. So it is necessary to study the transient characteristics in the starting process, but it is a great challenge faced by electrical machine designer.

In recent years, many researchers have extensively focused on the fluid field and/or temperature field of electrical motors under the steady-state and/or transient conditions. Boglietti proposed four thermal models based on the lumped-parameter thermal networks and evaluated the stator-winding temperature rise of an induction motor in short-time thermal transient condition [1]. Wallscheid and Böcker [2] analyzed the thermal behavior of a permanent magnet synchronous motor within a specific driving cycle based on a low-order lumped parameter thermal network. Bornschlegell *et al.* [3] calculated the temperature field of a high-power salient-pole electrical machine according to the coupling of a thermal network model and a flow calculation. Li *et al.* [4] proposed an electromagnetic-thermal optimization method to reduce the winding temperature rise of a permanent magnet brushless DC motor working in the short-time duty, but the coupling between thermal behavior and fluid motion is not taken into account. Han *et al.* [5], [6] built a 3D model of a large turbo generator and calculated the end part temperature. They also discussed the fluid flow and temperature when the turbo generator ran from the start to the steady-state operation [5], [6]. The temperature field of electrical machine has gained more

The associate editor coordinating the review of this manuscript and approving it for publication was Shuaihu Li.

TABLE 1. Basic parameters of HPDHV induction motor.

Rated power	Rated voltage	Rated speed	Ventilating duct width	Insulation class
2500 kW	6 kV	1480 r/min	8 mm	F

(a)

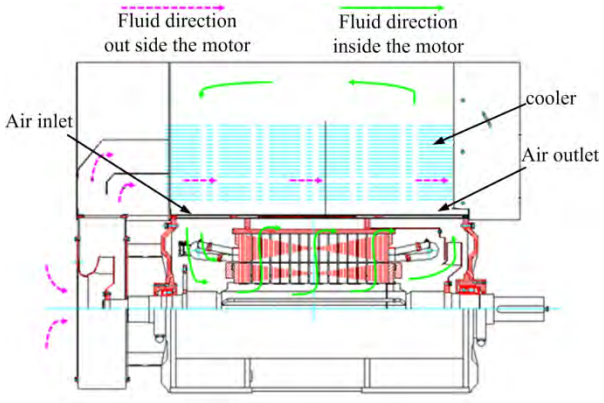

(b)

FIGURE 1. Structural representation of HPDHV induction motor. (a) Motor physical map. (b) Ventilation structure of the motor.

and more attention [7]–[10]. However, the physical fields of a HPDHV induction motor have been rarely reported, and the effects of the motor starting process on the fluid flow and the winding temperature rise of HPDHV induction motor need to be analyzed.

A HPDHV induction motor is studied in this paper. The accurate calculation of the heat generating and dissipating during the starting process of motor plays an important role in determining the transient temperature field. A 3D coupling model is proposed and is solved by considering the heat dissipation condition and the heat source. The temperature rise of induction motor in the starting process is analyzed when the induction motor runs with different loads. The proposed model is validated by experimental measurement.

II. ENTRANCE FLUID FLOW

The basic parameters of a YJKK500-4 HPDHV induction motor are shown in Table 1. The rated power is 2500 kW. The induction motor has 14 ventilation ducts. The ventilation system structure consisting of axial and radial ventilation ducts is shown in Fig. 1.

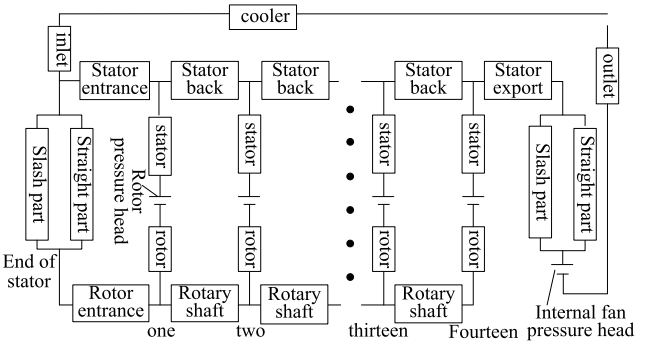

FIGURE 2. Equivalent wind resistance network model of the induction motor.

In order to calculate accurately the heat dissipation of the motor, the distribution of air volume in the motor and the wind speed should be known. The air volume is obtained by the equivalent airflow consisting of the wind resistance and the wind pressure source [11]. As the motor has a symmetric axial structure, only the 2D wind resistance network along the motor axial direction is studied. Fig. 2 illustrates the equivalent wind resistance network model of the motor. Any ventilation place inside the induction motor can be considered as a wind resistance. Among all the wind resistances, the wind resistances of the stator radial ventilation ducts mainly consists of four local wind resistances, namely, the one at the inlet of ventilation duct, the one at the stator teeth, the one extending from the stator teeth to the stator yoke, and the one at the stator yoke.

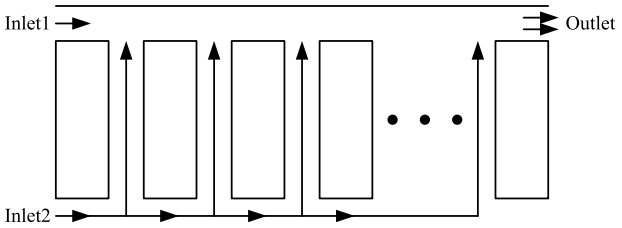

FIGURE 3. Flow direction of the airflow.

The flow direction of the airflow in the motor is shown in Fig. 3. Inlet1 and Inlet2 are the fluid inlets located near the stator back and the rotor field spider, respectively. The fluid inside the rotor field spider flows into the radial ventilation ducts under the centrifugal force, and then flows out from the stator back outlet. The inlet flow rate is obtained by solving the wind-resistance network model of motor [12], [13]. Under the rated speed, the axial fluid flow inside the rotor is calculated and is 0.922 m^3/s. The calculation results of fluid flow inside the radial ventilation ducts under the rated speed are shown in Fig. 4. We can see from Fig. 4 that the fluid flow inside the radial ventilation ducts increases with the ventilation-duct number, and Duct 1 has the lowest fluid flow of 0.039 m^3/s whereas Duct 14 has the highest fluid flow of 0.13 m^3/s. Since the cooling air at the rotor axial inlet has higher fluid flow and larger axial movement inertia, the radial fluid flow inside Duct 1 is very small. When the cooling air

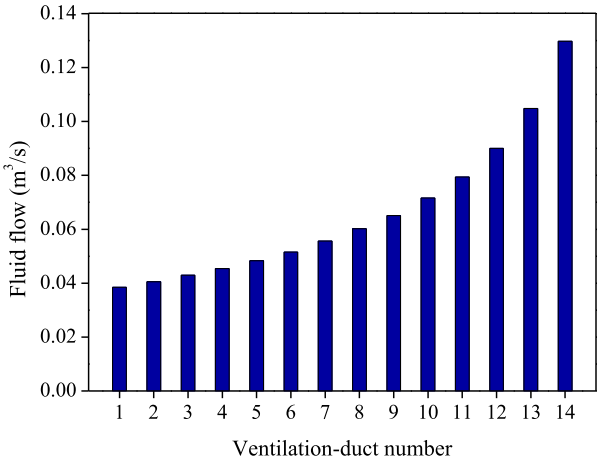

FIGURE 4. Fluid flow inside the radial ventilation ducts.

flows into the ventilation duct with a larger number, the axial fluid velocity decreases, and the fluid flow inside the radial ventilation duct increases gradually. Although the temperature of cooling air increases when the cooling air moves from the inlet to the outlet, the fluid flow of cooling air inside the ventilation ducts from the inlet to the outlet increases, which is helpful for the temperature balance of the induction motor along the axial direction.

The fluid flow in the radial ventilation duct under different rotating speed can be obtained by solving the wind resistance network, and it is nearly linear with the rotating speed. When the induction motor runs in a lower rotating speed, the wind pressure generated by the fan and rotor is smaller, and the fluid flow inside the ventilation duct caused by the centrifugal effect is also lower. With the increasing rotating speed, the fluid flow in the radial ventilation ducts is increased due to the centrifugal effect to enhance the cooling capacity.

III. TRANSIENT HEAT SOURCE

In the starting process, copper loss is the main heat source of the winding. The copper loss is related to the variable starting current. The copper loss (P_{Cu}) of the stator winding can be described as in

$$P_{Cu} = mI_{st}^2 R = m(I_{st}^* \cdot I_N)^2 R = I_{st}^* 2\left(mI_N^2 R\right) = I_{st}^* 2 P_{CuN} \tag{1}$$

where I_{st} is starting current. I_{st}^* is the ratio of starting current to the rated current. I_N is the rated current. P_{CuN} is the stator copper loss under the rated condition. R is the stator resistance. Thus, the copper loss in the starting process is mainly determined by the starting current.

The starting characteristics, such as the starting current and the rotating speed, can be obtained by the dynamic mathematical model of the induction motor. The dynamic mathematical model is described as follows [13], [14].

$$T_e = X_m\left(i_{T1}i_{M2} - i_{M1}i_{T2}\right) \tag{2}$$

$$H\frac{d\omega}{dt} = T_e - T_m \tag{3}$$

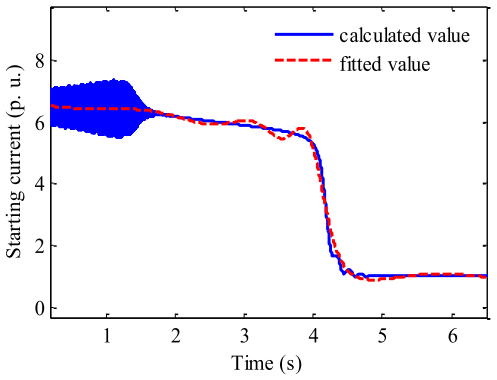

FIGURE 5. Starting current varying with time.

$$\frac{\mathrm{d}}{\mathrm{d}t}\begin{bmatrix} i_{M1} \\ i_{T1} \\ i_{M2} \\ i_{T2} \end{bmatrix} = \begin{bmatrix} X_{ss} & 0 & X_m & 0 \\ 0 & X_{ss} & 0 & X_m \\ X_m & 0 & X_{rr} & 0 \\ 0 & X_m & 0 & X_{rr} \end{bmatrix}^{-1} \left\{ \begin{bmatrix} u_{M1} \\ u_{T1} \\ 0 \\ 0 \end{bmatrix} + \begin{bmatrix} -r_1 & X_{ss} & 0 & X_m \\ -X_{ss} & -r_1 & -X_m & 0 \\ 0 & X_m & -r_2 & X_{rr} \\ -X_m & 0 & -X_{rr} & -r_2 \end{bmatrix} \begin{bmatrix} i_{M1} \\ i_{T1} \\ i_{M2} \\ i_{T2} \end{bmatrix} + \omega \begin{bmatrix} 0 & 0 & 0 & 0 \\ 0 & 0 & 0 & 0 \\ 0 & -X_m & 0 & -X_{rr} \\ X_m & 0 & X_{rr} & 0 \end{bmatrix} \begin{bmatrix} i_{M1} \\ i_{T1} \\ i_{M2} \\ i_{T2} \end{bmatrix} \right\} \tag{4}$$

where T_e is the electromagnetic torque. X_m is the magnetic inductance. i_{M1}, i_{T1}, i_{M2}, i_{T2} are two-phase current of stator and rotor, respectively. H is the inertia constant. ω is angular speed of rotor. T_m is the load torque. X_{ss}, X_{rr} are the self-inductances of stator and rotor, respectively. r_1 and r_2 are the resistances of the stator and rotor windings, respectively.

The calculation method described in [15] is used to determine the starting current characteristics and the dynamic impedance of the induction motor in the starting process. In the calculation procedure, the influences of saturation effect and skin effect on the impedance of the induction motor are also taken into account. The curves of the calculated values in Fig. 5 and Fig. 6 show the starting current characteristics and the rotating speed characteristics of the induction motor, respectively.

The starting current is used to evaluate the transient heat source boundary whereas the rotating speed is used to obtain the entrance flow rate by solving the wind resistance network model of the studied motor.

According to the calculated values shown in Fig.5 and Fig.6, respectively, the starting current ratio (I_{st}^*) and the rotating speed (n) are then fitted by (5) and (6). The fitted values of the starting current and rotating speed are also

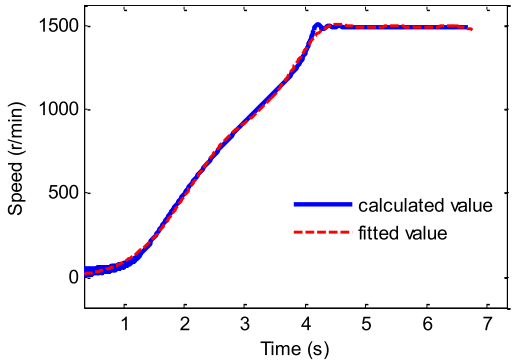

FIGURE 6. Rotating speed varying with time.

shown in Fig. 5 and Fig. 6, respectively.

$$I_{st}^{*} = 8.903e^{-\left(\frac{t+4.648}{7.579}\right)^2} - 1.966e^{-\left(\frac{t-4.086}{1.275}\right)^2} + 2.236e^{-\left(\frac{t-2.365}{1.886}\right)^2} + 2.475e^{-\left(\frac{t-3.399}{0.6936}\right)^2} + 2.556e^{-\left(\frac{t-3.938}{0.3001}\right)^2} \quad (5)$$

$$n = 573.9e^{-\left(\frac{t-4.319}{0.8312}\right)^2} + 1494e^{-\left(\frac{t-6.466}{2.66}\right)^2} + 112.8e^{-\left(\frac{t-5.383}{0.5368}\right)^2} + 613.7e^{-\left(\frac{t-2.81}{1.207}\right)^2} \quad (6)$$

where t is the starting time. Similarly, the calculation and fitting function of rotor starting current can be determined and are not repeated here.

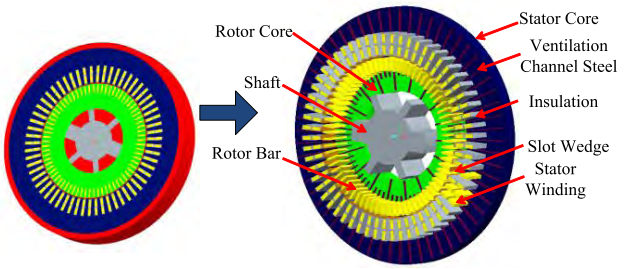

FIGURE 7. Fluid-solid coupling model of stator and rotor with one ventilation duct.

IV. FLUID-SOLID COUPLING MODEL AND SOLUTION

A. FLUID-SOLID COUPLING MODEL

Fig. 7 shows the 3D fluid-solid coupling model of stator and rotor, and the coupling model mainly consists of one ventilation duct, stator and rotor cores. Due to the symmetrical structure of the induction motor, 1/12 part of the 3D fluid-solid coupling model as shown in Fig. 7 is mainly studied to reduce the calculation amount and to improve the calculation efficiency. Fig. 8 shows the 1/12 part of the 3D coupling model, where S_1, S_2 and S_3 represent three different fluid inlets located at the stator back and rotor field spider, respectively.

B. BASIC ASSUMPTION AND COUPLING MODEL SOLUTION

As the symmetrical structure and heat transfer properties of the HPDHV induction motor, the following assumptions are made for the calculation of transient temperature field.

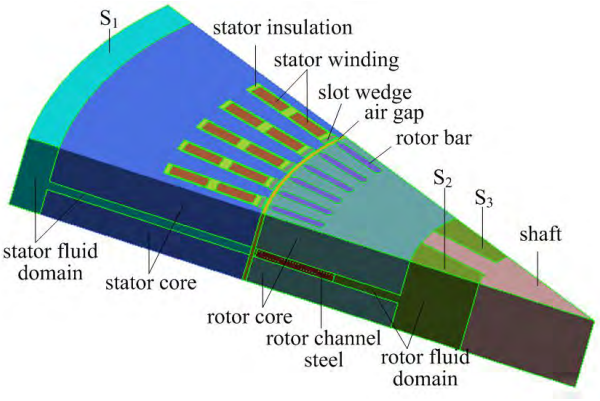

FIGURE 8. 1/12 fluid-solid coupling model of the induction motor.

1. All of the heat sources are the isothermal heating element.
2. At the initial time, the motor temperature is the same as the environment temperature and distribute uniformly.
3. The radiation heat transferring from the motor surface into the surrounding environment is few and can be neglected, and the environment temperature is considered to be constant all the time.
4. The influences of the airflow buoyancy and gravity are also neglected.
5. As the fluid velocity is far less than the acoustic velocity and the Mach number is relatively small, the fluid inside the induction motor is regarded as an incompressible fluid.
6. RNG k-ε turbulence model is applied, because the fluid inside the axial ventilation system has a large Reynolds number, and the rotor and bracket can be rotating. This turbulence model is based on Reynolds averaging method, and is defined as in [16], [17]

$$\begin{aligned} \rho\frac{\partial k}{\partial t} + \rho\frac{\partial (k\mu_i)}{\partial x_i} &= \frac{\partial}{\partial x_j}\left[\left(\mu + \frac{\mu_t}{\sigma_k}\right)\frac{\partial k}{\partial x_j}\right] + \Delta_k \\ \rho\frac{\partial \varepsilon}{\partial t} + \rho\frac{\partial (\varepsilon\mu_i)}{\partial x_i} &= \frac{\partial}{\partial x_j}\left[\left(\mu + \frac{\mu_t}{\sigma_\varepsilon}\right)\frac{\partial \varepsilon}{\partial x_j}\right] + \Delta_\varepsilon \end{aligned} \quad (7)$$

where ρ is the density. k is the turbulent kinetic energy. ε is the dissipation rate of the turbulence. μ is the kinetic viscosity. μ_t is the turbulent viscosity. μ_i is the velocity in the i^{th} direction. x_i and x_j are the i^{th} and j^{th} direction, respectively. Δ_k and Δ_ε are the addition items of the turbulence, respectively.

The 3D heat conduction mode in the solution domain is then defined as in

$$\begin{cases} \frac{\partial}{\partial x}\left(\lambda_x\frac{\partial T}{\partial x}\right) + \frac{\partial}{\partial y}\left(\lambda_y\frac{\partial T}{\partial y}\right) + \frac{\partial}{\partial z}\left(\lambda_z\frac{\partial T}{\partial z}\right) + q_v = \rho c\frac{\partial T}{\partial t} \\ -k_n\frac{\partial T}{\partial n} = \alpha\left(T - T_f\right) \end{cases} \quad (8)$$

where λ_x, λ_y, λ_z, k_n are the heat conductivity coefficients of the materials in x, y, z and n directions, respectively. T is the material temperature. c is the specific heat capacity. α is the heat transfer coefficient. T_f is the environmental temperature.

The losses of the induction motor running in the rated operation are experimentally measured and are shown in Table 2.

TABLE 2. Measurements of the motor losses under the rated operation.

Parameters	Values (W)
stator copper loss	15978
stator core loss	27819
stray loss	12940
no-load loss	39470
rotator copper loss	21916
Mechanical loss	10688

During the stating process, the heat values and rotating speed, which play a great effect on the temperature rise, are variable. According to (3) and (4), a user-defined function file is programmed to study the starting process characteristics. By calling the user-defined function, the rotor speed condition and the heat source are automatically set during the iterative calculation process.

According to these assumptions, the 3D fluid-solid coupling model as shown in Figure 8 is solved by the finite difference method [18] and the user-define functions combined with the determined heat dissipation boundary condition, the heat source and the measured losses.

V. CALCULATION AND RESULTS

A. FLUID VELOCITY VECTOR

Fig. 9 presents the fluid velocity vectors at 2, 3 and 4 s, respectively, when the motor is running with the rated load. The fluid velocity vectors as shown in Fig. 9 at different starting moment are similar. The rotation of rotor makes the fluid velocity in the rotor duct be higher than that in the stator duct. When the starting time is 4 s, the maximum fluid velocity is 48.6 m/s. In addition, the fluid velocity near the border between the rotor duct and the air gap is the highest, because the conducting bar in the rotor duct is the equal of the blades and drives the surrounding airflow. So, the fluid velocity increases with the rotating speed.

In Fig. 9, we also can observe that the fluid velocity does not distribute uniformly according to the center line of the stator slot. It is due to that the airflow driven by the rotating rotor flows into the stator duct with an angle. The used motor in this paper rotates in the counter-clockwise direction, so the fluid velocity near the left gear of the stator ventilation duct is much higher. In the starting process, the fluid velocity in the ventilation duct distributes non-uniformly along the radial direction of the stator winding. This is because the air pressure and the velocity of the airflow change greatly when the airflow flows from the narrow section into the expanding section.

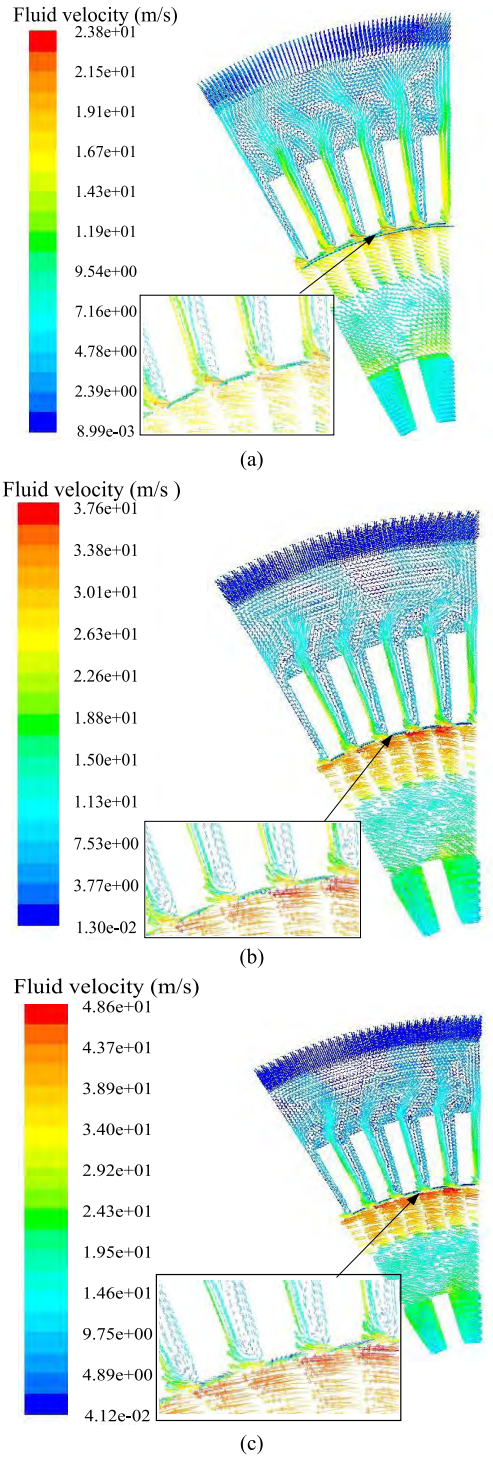

FIGURE 9. Fluid velocity vectors at different time. (a) 2 s, (b) 3 s and (c) 4 s.

B. TEMPERATURE RISE OF STATOR WINDING

The temperature distribution of motor at 3 and 4 s is shown in Fig. 10. It is indicated that the stator winding is the main heat source and the heat quantity focuses on the stator winding. Comparing with the stator winding, the temperature of the iron core is lower because of the less loss and the larger heat capacity of the iron core.

Since the rotating speed is lower in the initial starting process, the heat dissipation effect of the stator winding is not ideal and the highest temperature rise appears in the stator winding. Fig. 11 illustrates the highest temperature rise of the stator windings against time during the starting process, where the reference temperature is 300 K.

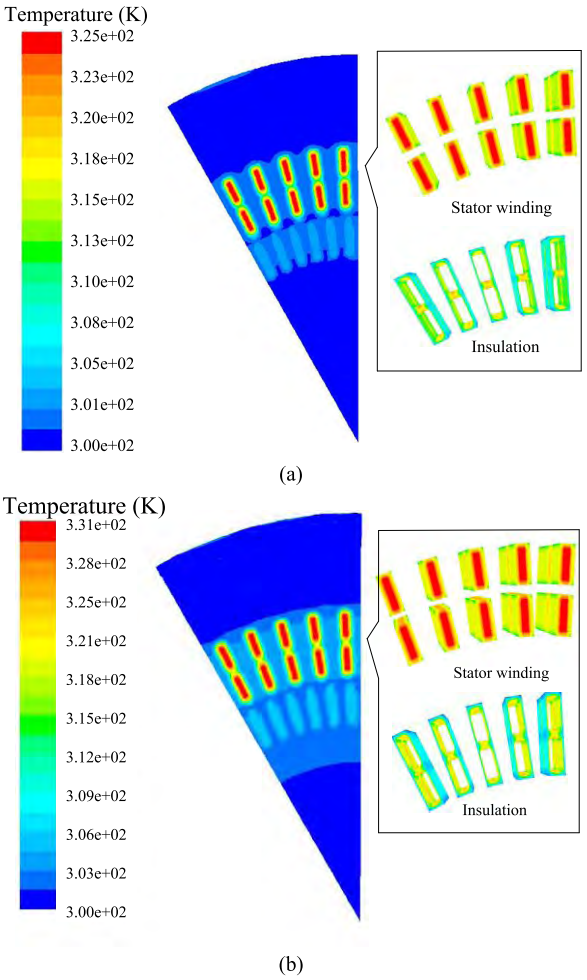

FIGURE 10. Temperature distributions inside the induction motor at (a) 3 s and (b) 4 s.

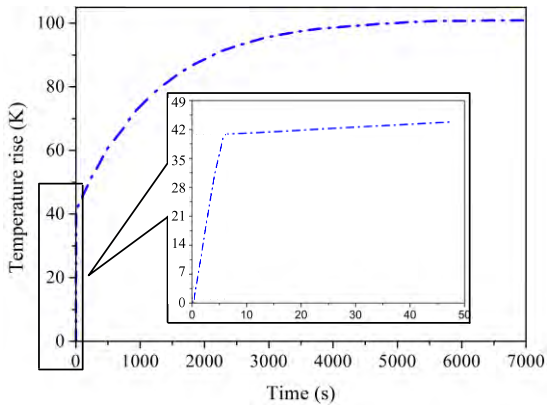

FIGURE 11. Highest temperature rise of the stator winding varying with time.

In Fig. 11, we can find that the winding temperature rise gradually increases with the running time, but the rates of temperature rise at different running time are different in the whole starting process. At the initial stage within 10 s as shown in the inset of Fig. 11, we can observe that the winding temperature rise increases much faster. During this initial

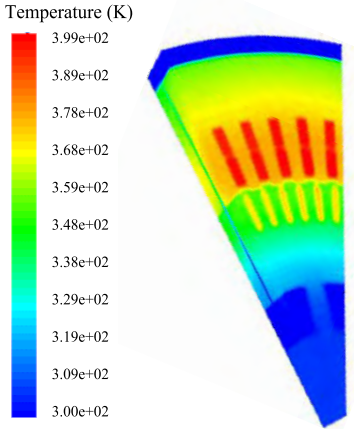

FIGURE 12. Temperature distributions inside the induction motor in the steady-state operation.

stage, the starting current in the stator and rotor windings is about six to seven times the rated current, but the rotating speed is much slower and the cooling condition inside the induction motor is poorer, so the winding temperature rise grows very rapidly. Just after the initial stage, the winding current decreases and the rotating speed is close to the synchronous speed. Meanwhile, the air pressure inside the induction motor increases and the fluid flow of cooling air in the axial and radial ventilation ducts also rises, leading to the augment of the cooling-air velocity. Subsequently, the winding temperature rise increase slowly within the time range from 10 to 5000 s as shown in Fig. 11. When the induction motor is running in the steady-state, the winding temperature rise keeps at a constant level. The steady-state temperature distribution inside the induction motor is shown in Fig. 12. We can learn that the maximum temperature rise is 99 K when the induction motor is running in the steady-state condition.

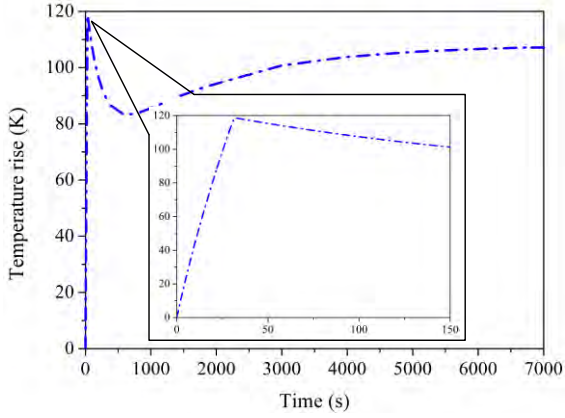

FIGURE 13. Maximum temperature rise against time when the load has1.5 times the rated load torque.

Fig. 13 shows the relationship between the stator-winding temperature rise and the running time when the induction motor is running with 1.5 times the rated load. At this operating condition, the induction motor has a much longer starting

time than the one running with the rated load. The winding current keeps a higher value for a longer time. In the starting process, the rotating speed fails to reach the rated value, and the fluid flow of cooling air is slow. The higher winding current and the poorer cooling effect lead to the fact that there is a large amount of heat accumulation in the winding and the winding temperature also increases rapidly.

In Fig. 13, we can see that the stator-winding temperature rise indeed increases rapidly in the starting process. The maximum stator-winding temperature rise is even close to 120 K as shown in the inset of Fig. 13. The stator-winding heating reduces when the current reaches the steady state, but the stator-iron-core temperature is still very low, so the heat transfer between the winding and the core makes the winding temperature rise decrease. Compared with the stator winding, the stator iron core has a larger specific heat and weight. In other words, the stator iron core has much larger heat capacity. The iron-core temperature rise changes significantly only when the heat quantity inside the iron accumulates to a certain extent. Due to the heating accumulation inside the iron core, the iron-core temperature increases and the motor gradually runs into thermal equilibrium. Therefore, as illustrated in Fig. 13, the stator-winding temperature rise reduces to a lowest value and then increases to the steady-state value, and the steady-state temperature rise of the windings is 107 K.

VI. EXPERIMENTAL VALIDATION

The accuracy of the calculation method for the starting characteristics (e.g., the starting current and the rotating speed) used in this paper can be verified by the analysis in [15]. The on-site test induction motor is shown in Fig. 14. Table 3 shows the calculation and experimental results, respectively. The on-site measured locked-rotor current is 6.35 times the rated current, whereas the calculated one by the proposed method is 6.44 times the rated current, the relative error is 1.42% and it meets the operation requirement.

In order to validate the accuracy and rationality of the proposed calculation method for the transient temperature rise, we carry out the experimental measurement of the steady-state temperature rise when the induction motor is running in the rated condition, and then compare the measurement results with the steady-state calculation results obtained by the proposed method. The on-site test induction motor is shown in Fig. 14. The PT100 double platinum thermal resistances are used as the temperature sensors. Several temperature sensors are applied at different positions on the stator windings, and the average temperature is used in this paper. Table III shows the measurement and calculation results of the temperature rise, respectively, when the induction motor is running in the rated steady-state condition. The relative error between the measurement value and the calculation value is 3.88% and is within the allowable range of the engineering practice. Furthermore, the result also proves that it is reliable for the proposed 3D fluid-solid coupling model and for the transient temperature calculation of the induction motor in the starting process.

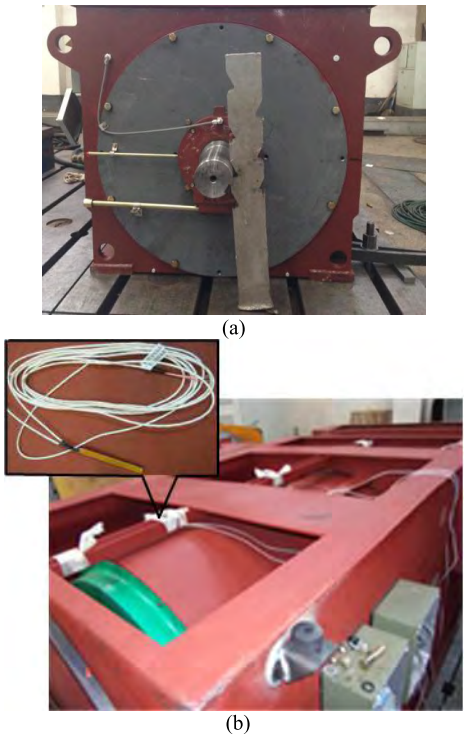

FIGURE 14. Locked-rotor and temperature measurement of the induction motor. (a) Locked rotor measurement. (b) temperature measurement.

TABLE 3. Calculations and experimental measurements results.

Parameters	Calculation	Measurement	Error
locked-rotor current	6.44 (p. u.)	6.35(p. u.)	1.42%
Temperature Rise	99(K)	95.3(K)	3.88%

VII. CONCLUSION

The heating critical region of the HPDHV induction motor is applied as the prototype of the 3D fluid-solid coupling model for the fluid flow and temperature rise when the induction motor is running in the starting process. The main conclusions are drawn as below.

1. The fluid flow in the ventilation ducts is obtained based on the wind resistance network. The fluid flow in the radial ventilation ducts increases from the inlet to the outlet. The total steady-state fluid flow inside the rotor is 0.922 m^3/s. The relationship between the fluid flow in the radial ventilation duct and the rotating speed is almost linear. The entrance fluid flow boundary conditions for the proposed model are also determined by the wind resistance network.

2. The starting current characteristics and the rotating speed characteristics of the induction motor are obtained according to the dynamic mathematical model. The heat source boundary condition for the 3D fluid-solid coupling model is derived by the curve fitting method.

3. The temperature rises of the induction motor which is running with different loads are obtained. The temperature rise may be very high when the induction motor is running

with much heavier load, which lays a theoretical foundation for further studying the induction motor under various working systems.

4. The comparison between the experimental results and the calculation results prove that the proposed method is feasible and reliable. This work is of great importance for the design and operation of HPDHV induction motor.

REFERENCES

[1] A. Boglietti, E. Carpaneto, M. Cossale, and S. Vaschetto, "Stator-winding thermal models for short-time thermal transients: Definition and validation," *IEEE Trans. Ind. Electron.*, vol. 63, no. 5, pp. 2713–2721, May 2016.

[2] O. Wallscheid and J. Böcker, "Global identification of a low-order lumped-parameter thermal network for permanent magnet synchronous motors," *IEEE Trans. Energy Convers.*, vol. 31, no. 1, pp. 354–365, Mar. 2016.

[3] A. S. Bornschlegell, J. Pelle, S. Harmand, A. Fasquelle, and J.-P. Corriou, "Thermal optimization of a high-power salient-pole electrical machine," *IEEE Trans. Ind. Electron.*, vol. 60, no. 5, pp. 1734–1746, May 2013.

[4] Q. Li, M. Dou, B. Tan, H. Zhang, and D. Zhao, "Electromagnetic-thermal integrated design optimization for hypersonic vehicle short-time duty PM brushless DC motor," *Int. J. Aerospace Eng.*, vol. 2016, pp. 1–9, Aug. 2016.

[5] J. Han, B. Ge, D. Tao, and W. Li, "Influence of cooling fluid parameter on the fluid flow and end part temperature in end region of a large turbogenerator," *IEEE Trans. Energy Convers.*, vol. 31, no. 2, pp. 466–476, Jun. 2016.

[6] H. Jichao, G. Baojun, T. Dajun, Z. Hongsen, X. Fang, and W. Li, "Calculation and analysis of complex fluid flow and thermal fields in a fully air-cooled hydrogenerator," *Int. J. Therm. Sci.*, vol. 116, pp. 278–286, Jun. 2017. doi: 10.1016./j.ijthermalsci.2017.02.013.

[7] P. Zhang, Y. Du, T. G. Habetler, and B. Lu, "Improving thermal recovery time for soft-starter-connected ac motors with intermittent periodic duty cycles," *IEEE Trans. Ind. Appl.*, vol. 46, no. 5, pp. 1927–1935, Sep./Oct. 2010.

[8] S. Li, N. A. Gallandat, J. R. Mayor, T. G. Habetler, and R. G. Harley, "Calculating the electromagnetic field and losses in the end region of a large synchronous generator under different operating conditions with 3-d transient finite-element analysis," *IEEE Trans. Ind. Appl.*, vol. 54, no. 4, pp. 3281–3293, Jul./Aug. 2018.

[9] W. Li, J. Cao, F. Huo, and J. Shen, "Numerical analysis of stator-rotor coupled transient thermal field in induction motors with blocked rotor," in *Proc. World Autom. Congr.*, Hawaii, HI, USA, Sep./Oct. 2008, pp. 1–6.

[10] S. Zhu, M. Cheng, and X. Cai, "Direct coupling method for coupled field-circuit thermal model of electrical machines," *IEEE Trans. Energy Convers.*, vol. 33, no. 2, pp. 473–482, Jun. 2018.

[11] R. Yabiku, R. Fialho, L. Teran, M. E. Ramos, and N. Kawasaki, "Use of thermal network on determining the temperature distribution inside electric motors in steady-state and dynamic conditions," *IEEE Trans. Ind. Appl.*, vol. 46, no. 5, pp. 1787–1795, Sep./Oct. 2010.

[12] Y. Xia, D. Meng, and Y. Xu, "Calculation for the heating and safe operation time of YKK series highvoltage motors in starting process," *Open Elect. Electron. Eng. J.*, vol. 7, no. 1, pp. 39–45, 2013.

[13] B. Ge, X. Xu, D. Tao, J. Han, and L. Wang, "Gas friction loss in stator ventilation ducts of the drive motor for the cooling medium in a high-temperature gas-cooled reactor," *IEEE Trans. Ind. Electron.*, vol. 66, no. 1, pp. 114–123, Jan. 2019.

[14] X. Liang, W. Xu, C. Y. Chung, W. Freitas, and K. Xiong, "Dynamic load models for industrial facilities," *IEEE Trans. Power Syst.*, vol. 27, no. 1, pp. 69–80, Feb. 2012.

[15] D. Meng, Y. Xia, and Y. Xia, "Engineering calculation of dynamic impedances and starting characteristics for high-voltage induction motors," *Int. Trans. Elect. Energy Syst.*, vol. 25, no. 5, pp. 920–932, 2014.

[16] J. Wen and J. Zheng, "Numerical analysis of the external wind path for medium-size high-voltage asynchronous motors," *Appl. Therm. Eng.*, vol. 90, pp. 869–878, Nov. 2015.

[17] Y. Xiwei and M. Dawei, "Design analysis and improvement of cooler in positive-pressure explosion-proof low-speed high-capacity induction motors," *Appl. Therm. Eng.*, vol. 129, pp. 1002–1009, Jan. 2018.

[18] L. Wang and W. Li, "Assessment of the stray flux, losses, and temperature rise in the end region of a high-power turbogenerator based on a novel frequency-domain model," *IEEE Trans. Ind. Electron.*, vol. 65, no. 6, pp. 4503–4513, Jun. 2018.

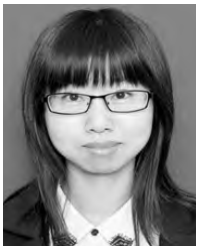

YUNYAN XIA was born in Heilongjiang, China, in 1987. She received the B.S., M.S., and Ph.D. degrees in electrical machinery and appliance from the Harbin University of Science and Technology, Harbin, in 2009, 2012, and 2014, respectively, where she is currently a Lecturer. Her research interests include synthesis physical fields and dynamic operation mechanism of special electric machines, particularly in high-power-density and high-voltage induction motors.

YONGSEN HAN was born in Heilongjiang, China, in 1985. He received the Ph.D. degree in electrical engineering from Xi'an Jiaotong University (XJTU), China, in 2018. He is currently a Lecturer with the Harbin University of Science and Technology. His research interests include the measurement and electrical properties of nonlinear insulating materials.

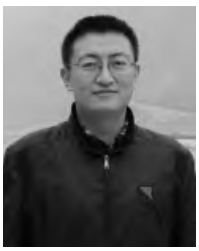

YONGMING XU was born in 1976. He received the Ph.D. degree in electrical machinery and appliance from the Harbin University of Science and Technology, Harbin, in 2008. He has published more than 30 academic papers and 3 books. He holds more than ten patents. His research interests include design of special motor, numerical calculation of integrated physical field in motor, and research on local overheating and fluid field of super large transformer.

MENGMENG AI was born in Heilongjiang, China, in 1991. He has published 11 academic papers (which more than 9 papers were included by SCI and EI). He holds ten patents. His research interests include optimal design of motor, numerical calculation of integrated physical field in motor, and research on local overheating and fluid field of super large transformer.